*J. Fluid Mech.* (2025), *vol.* 1017, A22, doi:10.1017/jfm.2025.10476

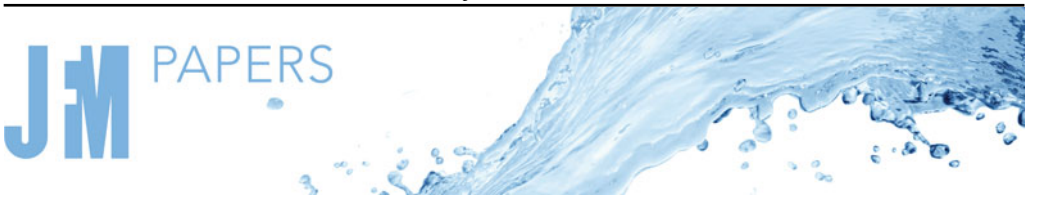


# A laboratory study of wave-induced drift under rotation

**J. Mol**[1], **P.M. Bayle**[1], **M. Duran-Matute**[2] **and T.S. van den Bremer**[1]

[1]Faculty of Civil Engineering and Geosciences, Delft University of Technology, 2628 CD Delft, The Netherlands

[2]Department of Applied Physics and Science Education, Eindhoven University of Technology, PO Box 513, 5600 MB Eindhoven, The Netherlands

**Corresponding author:** J. Mol, j.mol@tudelft.nl

(Received 10 January 2025; revised 15 May 2025; accepted 14 July 2025)

Waves transport particles in the direction of wave propagation with the Stokes drift. When the Earth's rotation is accounted for, waves induce an additional (Eulerian-mean) current that reduces drift and is known as the anti-Stokes drift. This effect is often ignored in oceanic particle-tracking simulations, despite being important. Although different theoretical models exist, they have not been validated by experiments. We conduct laboratory experiments studying the surface drift induced by deep-water waves in a purpose-built rotating wave flume. With rotation, the Lagrangian-mean drift deflects to the right (counterclockwise rotation) and reduces in magnitude. Compared with two existing steady theoretical models, measured drift speed follows a similar trend with wave Ekman number but is larger. The difference is largely explained by unsteadiness on inertial time scales. Our results emphasise the importance of considering unsteadiness when predicting and analysing the transport of floating material by waves.

**Key words:** waves in rotating fluids, surface gravity waves, ocean processes

## 1. Introduction

Understanding particle transport in the ocean is crucial for predicting the distribution of nutrients (Gruber *et al.* 2011), plankton (Nooteboom *et al.* 2019) and pollutants including plastic litter (van Sebille *et al.* 2020) as well as for search-and-rescue operations (Breivik *et al.* 2013). Particle transport is influenced by processes over a wide range of scales, from large-scale ocean gyres to small-scale turbulent mixing (Sutherland *et al.* 2023). One of the important processes for particles floating on or suspended near the ocean surface is

transport due to surface gravity waves. Such particles experience a net drift in the wave direction known as Stokes drift (Stokes 1847; van den Bremer & Breivik 2017). Including Stokes drift in particle-tracking simulations significantly changes their pathways and final distribution. In the Indian Basin, it results in leakage of particles into the South Atlantic instead of the South Pacific (Dobler *et al.* 2019). Taking into account Stokes drift also leads to increased transport to Arctic regions (Fraser *et al.* 2018; Onink *et al.* 2019).

However, the velocity with which (small) particles are transported by waves is not the Stokes drift but the (wave-induced) Lagrangian-mean velocity:

$$\overline{\boldsymbol{u}}_L = \boldsymbol{u}_S + \overline{\boldsymbol{u}}_E, \tag{1.1}$$

where $\overline{\{\}}$ denotes a wave average, $\boldsymbol{u}_S$ is the Stokes drift and $\overline{\boldsymbol{u}}_E$ the wave-induced Eulerian-mean velocity. For periodic waves in a non-rotating reference frame with zero viscosity, Stokes drift is the only contribution to the wave-induced Lagrangian-mean transport (Stokes 1847) (i.e. $\overline{\boldsymbol{u}}_E = 0$). In addition to Stokes drift, waves induce a Eulerian-mean velocity in three circumstances, which we explain below.

First, when the wave field varies spatially, an Eulerian-mean velocity forms, known as the return flow underneath wave groups (Longuet-Higgins & Stewart 1962; McIntyre 1981) or the undertow when waves shoal near coasts (Lentz & Fewings 2012). Second, in wave-driven boundary layers, viscosity causes an Eulerian-mean velocity in a process known as boundary-layer streaming (Longuet-Higgins 1953; Phillips 1977), known for transporting sediment at the sea bed (Nielsen 2006). In the turbulent upper-ocean boundary layer, the interaction between turbulence and Stokes drift can instead lead to an Eulerian-mean flow opposing the Stokes drift, as demonstrated in large-eddy simulations (Pearson 2018). Third, when background rotation is present, a wave-induced Eulerian-mean flow, known as the anti-Stokes drift, can emerge and exactly cancel the Stokes drift (Hasselmann 1970). On a rotating Earth, the Lagrangian-mean flow is deflected to the right of the Stokes drift (Northern Hemisphere) and takes the form of an inertial oscillation that averages to zero over the inertial period for periodic waves when ignoring viscosity (Ursell 1950; Hasselmann 1970). To explain this further, Pollard (1970) derived Gerstner-wave-like solutions on a rotating Earth without viscosity that display zero Lagrangian-mean drift (see also Weber 2011). In the Craik–Leibovich equations, which describe how waves affect ocean circulation, this is captured by the Coriolis–Stokes force (Craik & Leibovich 1976; Huang 1979; Suzuki & Fox-Kemper 2016).

Recently, wave-induced Eulerian-mean flows due to the Earth's rotation have been included in models for particle transport. Taking the time-dependent solution to the Ekman–Stokes equations by Higgins, Vanneste & van den Bremer (2020), Cunningham, Higgins & van den Bremer (2022) showed that adding the wave-induced Eulerian-mean flow has a substantial effect on the global distribution of floating marine plastic. Fully coupled wave–ocean models can also be used to study the effect of the wave-induced Eulerian-mean velocity (Drivdal, Broström & Christensen 2014; Rühs *et al.* 2024). The exact form of the wave-induced Eulerian-mean velocity depends crucially on the boundary condition applied at the free surface, which is not at all obvious *a priori* and depends on assumptions about the applied forcing (Weber 2019).

In the field, several measurement campaigns also suggest the existence of wave-induced Eulerian-mean flows potentially explained by the Earth's rotation. Smith (2006) measured Eulerian-mean 'counterflows' that cancelled the variation of the Stokes drift due to deep-water wave groups. Lentz *et al.* (2008) observed Eulerian-mean velocity profiles over the inner shelf with a vertical structure similar to that of the Stokes drift but with opposite direction (i.e. anti-Stokes drift). Röhrs *et al.* (2012) used estimates from field data in northern Norway to show that the Coriolis–Stokes force was of similar magnitude

to the ordinary Coriolis force. Additionally, inertial oscillations were observed in their drifter measurements. Ardhuin *et al.* (2009) have also obtained the Eulerian-mean (wave-induced) current from measurements and compared this to a model that includes the effect of the Coriolis–Stokes force.

In understanding wave-induced flows, laboratory experiments have played a crucial role (Paprota, Sulisz & Reda 2016; van den Bremer & Breivik 2017; Lenain, Pizzo & Melville 2019; van den Bremer *et al.* 2019; Monismith 2020). Wave-induced Eulerian-mean flows have led to considerable difficulty in reconciling laboratory observations with theoretical predictions of drift (Monismith *et al.* 2007), which can often be explained by complex boundary conditions imposed by laboratory flumes (van den Bremer & Breivik 2017). For finite-duration wave groups, boundary layers do not have time to develop and Eulerian-mean flows that agree with (potential-flow) theory have been observed in the laboratory (van den Bremer *et al.* 2019; Monismith 2020). The effect of rotation on drift has not been studied in the laboratory before.

In this paper, we develop and employ a novel laboratory set-up to study wave-induced drift of periodic deep-water waves under the effect of rotation. By varying the rotation rate, we can study, at the laboratory scale, the effects of rotation that would otherwise only arise at very large (inertial) scales in the field. We compare the results with existing theoretical models that make different assumptions about the boundary condition at the surface and thus assess their suitability for predicting particle transport in the ocean.

## 2. Methodology

### 2.1. *Experimental set-up and parameter space*

To study the effect of rotation at the laboratory scale, we place a wave flume on top of a rotating table with a diameter of 1.7 m (figure 1). The flume is 2.2 m long, 0.5 m wide and 0.3 m high with a water depth of $h = 0.15$ m. A video of the set-up during a measurement is included as supplementary movie 1 (available at https://doi.org/10.1017/jfm.2025.10476). To reduce surface contamination and capillary ripples, 1.4 ml of wetting agent was added to the water every time the flume was filled (as done by, for example, Swan & Sleath (1990)). Due to the small amount, the wetting agent does not have any other major effects on the flow. A transparent lid on top of the wave flume minimised airflow (and drift thus induced). A flap-type wavemaker controlled using linear wave theory was used to generate periodic waves. At the other end of the flume, a porous wave-absorbing beach was placed, consisting of 2–4 mm gravel stones glued together to form a 1/3.5 slope. The surface elevation was measured at seven different points using resistance-type wave gauges recording at 128 Hz.

To measure particle drift, yellow polypropylene (density $\sim 0.92$ g cm$^{-3}$) spherical particles with a diameter of 2 mm were dropped on the water surface. A particle-dropping system ensured that they were consistently dropped at the same locations, with a spacing of 6 cm. The position of the floating particles was recorded using a downward-looking camera with a resolution of $3840 \times 2160$ pixels, recording at 29.97 frames per second. The camera was mounted 1.3 m above the water surface with a 25 mm lens, giving a field of view of 95 c$m \times 54$ cm, which was illuminated by LED panels on each side of the flume. The particles were large enough to be clearly visible in the images (with a diameter of $\sim 10$ pixels) and small enough to be able to ignore the effects of the particle size on their drift (Calvert *et al.* 2024).

Waves were generated with frequencies $f_w = 2.6$, 2.8 and 3.0 Hz and amplitudes 7.0 mm $\leqslant a \leqslant$ 8.2 mm for six different rotation rates $\Omega$ ranging from 0 to 0.42 rad s$^{-1}$ (see table 1). The rotation rate was always such that $2\Omega/\omega \ll 1$ (with $\omega$ the angular

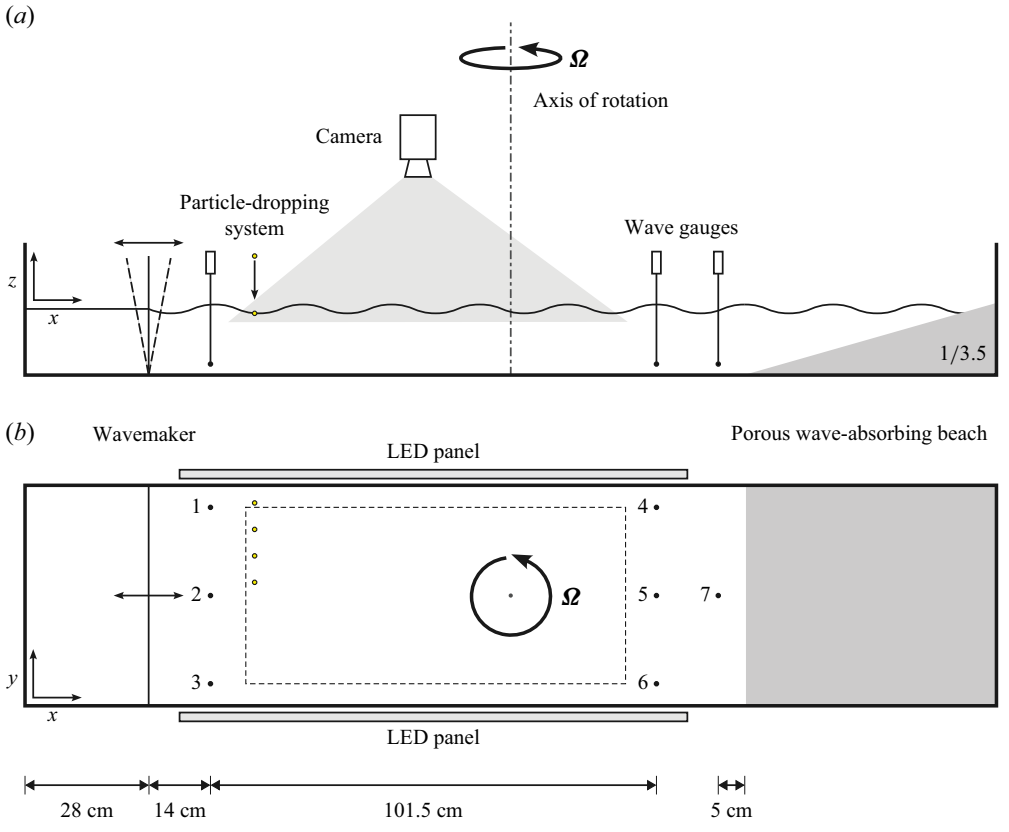


Figure 1. Schematic of the laboratory set-up placed on a rotating table, showing side view (*a*) and top view (*b*). The dashed rectangle indicates the region of interest where drift is measured. Numbered black dots indicate the wave gauges and yellow dots the particle-dropping locations.

frequency of the wave) as required by the theoretical models with which we will compare. The dimensional parameters above are chosen to reliably measure drift in the laboratory and to obtain values of the relevant non-dimensional parameters that encompass realistic ocean conditions. All experiments are within the deep-water regime with $4.0 \leqslant kh \leqslant 5.4$, where $k$ is the wavenumber. The steepness of the waves $ka$ is large compared with typical ocean waves ($0.21 \leqslant ka \leqslant 0.26$), as this allows us to distinguish the wave-induced drift from Eulerian-mean background flows that are not induced by the waves but by, for instance, small temperature gradients in the laboratory, air flow over the flume and Eulerian-mean flows from previous experiments that decay slowly (that is, those associated with longer spatial scales). The (inverse) wave Ekman number (Huang 1979), $0 \leqslant Ek^{-1} = \Omega/(4\nu k^2) \leqslant 1.4 \times 10^2$, where $\nu$ is the viscosity, encompasses most realistic ocean conditions (see § 5).

### 2.2. *Measurement procedure*

To minimise wave generation due to spin up, the rotation rate $\Omega$ was gradually increased to the desired value with an acceleration of 0.01 rad s$^{-2}$. The e-folding time scale associated with adjustment to rigid-body rotation is the Ekman time scale $t_E = h/\sqrt{\nu\Omega}$ (Greenspan & Howard 1963; Vallis 2017). We waited $5t_E$ (i.e. between 19 and 55 min, using $\nu = 10^{-6}$ m$^2$ s$^{-1}$) before starting wave generation (see table 2 in Appendix A.1). The

| Frequency $f_w$ (Hz) | Amplitude $a$ (mm) | Rotation rate $\Omega$ (rad s$^{-1}$) | Water depth $h$ (cm) | Steepness $ka$ | Relative depth $kh$ | Relative rotation $2\Omega/\omega$ ($10^{-2}$) | Repeat |
|---|---|---|---|---|---|---|---|
| 2.6 | 7.8 ± 0.5 | 0.4189 | 14.8 | 0.21 | 4.0 | 5.1 | ∗ † ‡ |
| 2.6 | 8.1 ± 0.6 | 0.3142 | 14.9 | 0.22 | 4.1 | 3.8 | † |
| 2.6 | 8.1 ± 0.7 | 0.2094 | 14.9 | 0.22 | 4.1 | 2.6 | † |
| 2.6 | 8.2 ± 0.9 | 0.1047 | 15.0 | 0.22 | 4.1 | 1.3 | † |
| 2.6 | 7.9 ± 1.1 | 0.0524 | 15.0 | 0.21 | 4.1 | 0.6 | ∗ |
| 2.6 | 8.0 ± 0.3 | 0.0000 | 15.0 | 0.22 | 4.1 | 0.0 | ∗ † |
| 2.8 | 7.6 ± 0.5 | 0.4189 | 14.8 | 0.24 | 4.7 | 4.8 | |
| 2.8 | 7.6 ± 0.6 | 0.3142 | 14.9 | 0.24 | 4.7 | 3.6 | |
| 2.8 | 7.6 ± 0.7 | 0.2094 | 14.9 | 0.24 | 4.7 | 2.4 | |
| 2.8 | 7.6 ± 0.9 | 0.1047 | 15.0 | 0.24 | 4.7 | 1.2 | |
| 2.8 | 7.7 ± 1.2 | 0.0524 | 15.0 | 0.24 | 4.7 | 0.6 | |
| 2.8 | 7.4 ± 0.2 | 0.0000 | 15.0 | 0.23 | 4.7 | 0.0 | |
| 3.0 | 7.1 ± 0.5 | 0.4189 | 14.8 | 0.26 | 5.4 | 4.4 | |
| 3.0 | 7.3 ± 0.8 | 0.3142 | 14.9 | 0.26 | 5.4 | 3.3 | |
| 3.0 | 7.1 ± 0.8 | 0.2094 | 14.9 | 0.26 | 5.4 | 2.2 | |
| 3.0 | 7.2 ± 1.2 | 0.1047 | 15.0 | 0.26 | 5.4 | 1.1 | |
| 3.0 | 7.0 ± 1.2 | 0.0524 | 15.0 | 0.25 | 5.4 | 0.6 | |
| 3.0 | 7.1 ± 0.2 | 0.0000 | 15.0 | 0.26 | 5.4 | 0.0 | |

Table 1. Overview of the experiments with relevant parameters. The standard deviation in the average measured wave amplitude $a$ is calculated from the amplitudes measured at each of the wave gauges. A repeat without any change is indicated with ∗. A repeat where the wave gauges have been removed is indicated with †. A repeat with the same rate of the rotation but in the opposite direction (negative rotation rate) is indicated with ‡. A positive value of the rotation rate denotes counterclockwise rotation of the table while a negative value denotes clockwise rotation.

centrifugal effect of rotation causes a parabolic deformation of the free surface with the lowest level at the centre of rotation. To keep the water level at the wavemaker constant for all experiments, the non-rotating water depth was adjusted between 14.8 and 15.0 cm.

To obtain particle trajectories, a video recording was started at 5, 20, 35 and 50 min after the start of wave generation. During each video, approximately 32 particles were dropped in lines of four at 1 min intervals. The particles were dropped at the beginning of the measurement area near the wall on the left side with respect to the wave direction for counterclockwise rotation, or near the right side for clockwise rotation. The recording was stopped after 12 min or when all particles had moved outside of the field of view. For the non-rotating experiments, instead of a spin-up time, we let the wave flume rest for 20 min before starting wave generation. For these experiments, the particles are dropped in lines of eight that cover the full width of the flume, but the total number of particles remains 32. See figure 5 in Appendix A.2 for a detailed measurement timeline.

Particles are tracked within the region of interest, located 5 cm away from each of the sidewalls (figure 1), with the CSRT (Channel and Spatial Reliability Tracking) algorithm using the OpenCV Python library. Tracks that are too short and parts of tracks where tracking is lost are discarded (see Appendix A.3 for further details). Due to these selection criteria and imperfections in the particle dropping, the number of particles per video for which we can find a drift velocity can differ from 32.

## 3. Theory

A particle's motion is affected by processes on several time scales. On the time scale of the wave period, the particle moves forward with the crest of the wave and backwards with the

trough. When we average the velocity of the particle over this fast time scale, we obtain the Lagrangian-mean or drift velocity $\overline{\boldsymbol{u}}_L$. This drift velocity can vary on slower time scales, such as the one provided by the inertial period of the reference frame in which the waves propagate, $2\pi/f$ with $f = 2\Omega$ the Coriolis parameter. Under specific idealisations, i.e. an infinitely long wave flume in a non-rotating reference frame ($\Omega = 0$) with zero viscosity and ignoring spatial variation of the wave field, the theoretical wave-induced Lagrangian-mean velocity is given by the Stokes drift (i.e. $\overline{\boldsymbol{u}}_L = \boldsymbol{u}_S$ with $\overline{\boldsymbol{u}}_E = 0$), which is in the direction of the waves and has magnitude (Stokes 1847)

$$|\boldsymbol{u}_S| = \omega a^2 k \mathrm{e}^{2kz} \tag{3.1}$$

in the deep-water regime, with $z$ the vertical coordinate, defined positive upwards from the still-water level.

In a rotating reference frame ($\Omega \neq 0$) and with non-zero viscosity, the wave-induced Eulerian-mean velocity is non-zero (i.e. $\overline{\boldsymbol{u}}_E \neq 0$ and $\overline{\boldsymbol{u}}_L = \boldsymbol{u}_S + \overline{\boldsymbol{u}}_E$). A number of theories have been developed for wave-induced transport that include the effect of rotation and viscosity. These theories assume an infinite spatial domain and, therefore, do not account for the effects on the drift velocity of the finite length and lateral boundaries of a wave flume. They also assume small wave steepness and slow rotation ($2\Omega/\omega \ll 1$) and neglect capillary effects. Additionally, assumptions are made on the forcing of the wave field, in which we can distinguish two fundamentally different approaches. In what we term unforced models (Madsen 1978), which are based on the classical boundary-layer (and wave-stress) analysis of Longuet-Higgins (1953), no explicit forcing is put in place to ensure that the wave field is of permanent form, whilst its viscous decay is implicitly ignored (§ 3.1). In what we term forced models (Weber 1983), an oscillating wind stress (normal to the surface) exactly compensates the viscous attenuation of the wave field (§ 3.2). As a consequence, the models predict different wave-induced Lagrangian-mean velocities. While these velocities, in principle, still vary on the time scale of rotation, further averaging over the inertial period is typically assumed (steady drift prediction; §§ 3.1, 3.2), although this is not required (unsteady; § 3.3).

### 3.1. *Unforced–steady model*

As a first case, all time dependence is neglected (steady) and the wave is assumed not to be forced by any stress on the surface (unforced) by applying the boundary condition of Longuet-Higgins (1953) and Ünlüata & Mei (1970). In this case, the Lagrangian-mean velocity is given by (Madsen 1978; Xu & Bowen 1994; Seshasayanan & Gallet 2019)

$$\overline{\overline{U}}_L(z) = \frac{u_S|_{z=0}}{\sqrt{2\mathrm{i}\, Ek^{-1}}}\left(1 - \frac{2\mathrm{i}\, Ek^{-1}}{1 - 2\mathrm{i}\, Ek^{-1}}\right)\mathrm{e}^{(1+\mathrm{i})z/\delta_E} + \frac{u_S(z)}{1 - 2\mathrm{i}\, Ek^{-1}}, \tag{3.2}$$

where $u_S$ is the Stokes drift for waves that travel in the $x$ direction and we use the complex notation $U_L = u_L + \mathrm{i}v_L$, with $u$ and $v$ the velocities in the $x$ and $y$ directions, respectively. The average over the wave and inertial periods is denoted by $\overline{\overline{\{\}}}$. At $z = 0$, where we evaluate all theoretical models to compare with experiments, $\overline{\overline{U}}_L/u_S$ only depends on the (inverse) wave Ekman number, defined as $Ek^{-1} = \delta_S^2/\delta_E^2 = \Omega/(4\nu k^2)$, with the Stokes depth $\delta_S = 1/(2k)$ and the Ekman depth $\delta_E = \sqrt{2\nu/f}$ (Huang 1979). The (inverse) wave Ekman number, $Ek^{-1}$, is an inverse Ekman number with the characteristic length scale set to the Stokes depth; it determines the relative importance of rotation and viscosity.

Including the effect of rotation as in (3.2) causes a particle to drift to the right of the wave direction for counterclockwise rotation (figure 2*b*,*c*) or to its left for clockwise rotation (figure 2*d*). Increasing the (inverse) wave Ekman number reduces the magnitude

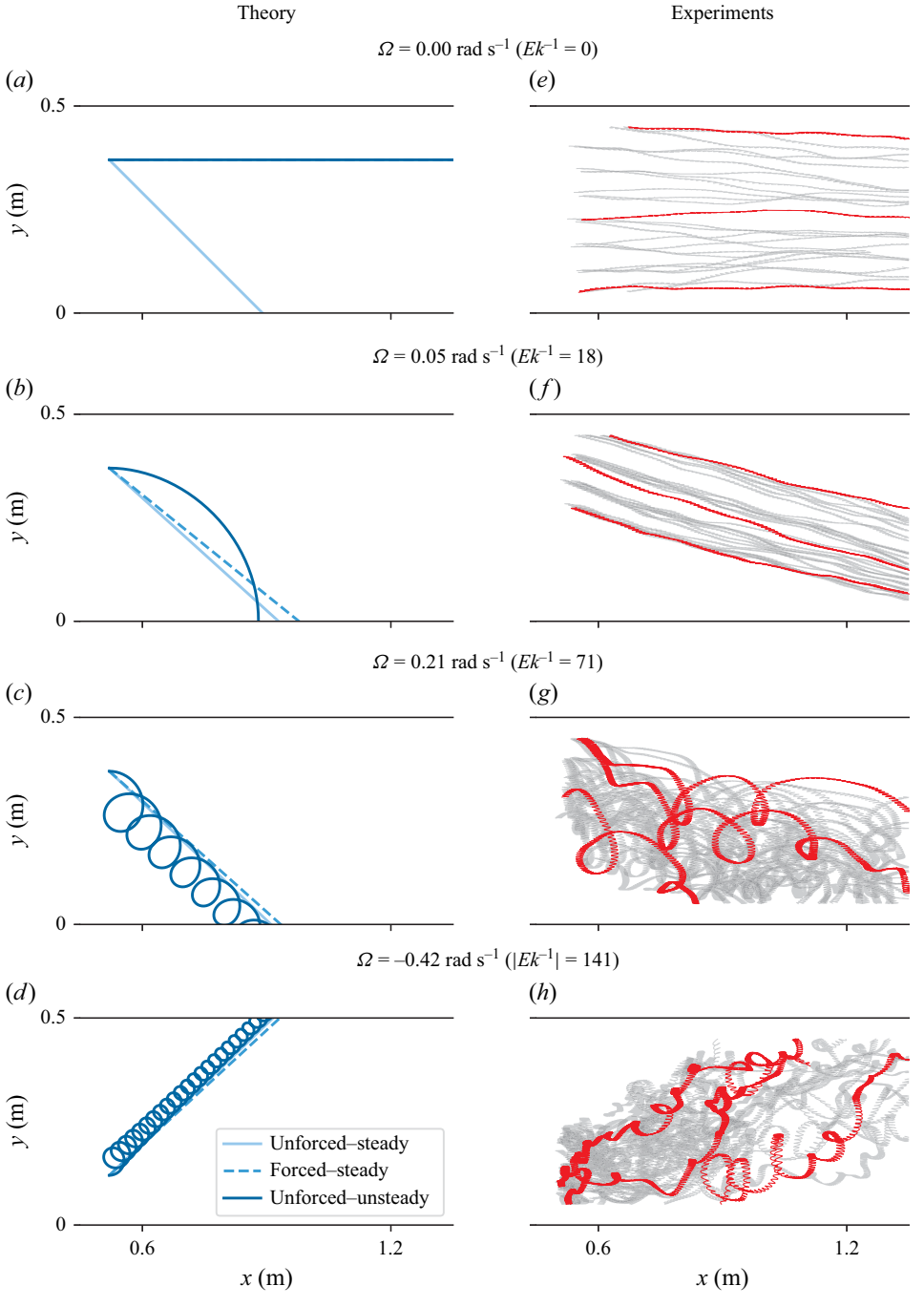


Figure 2. Particle trajectories for experiments with waves travelling in the $x$ direction with a frequency $f_w = 2.6$ Hz and subjected to different rotation rates $\Omega$ and thus (inverse) wave Ekman numbers $Ek^{-1}$. (*a–d*) The theoretical particle trajectory at the surface ($z = 0$) predicted by the three different models. (*e–h*) All trajectories measured in the flume during a single video measurement, where three example trajectories are highlighted in red.

of the drift $|\overline{\overline{\boldsymbol{u}}}_L|$ with $|\overline{\overline{\boldsymbol{u}}}_L| \to 0$ as $Ek^{-1} \to \infty$. Equation (3.2) thus predicts complete compensation of the Stokes drift by the 'anti-Stokes drift' in the rapid-rotation limit. The combined assumptions of a steady state for an unforced wave field in infinitely deep water cause this solution to tend to infinity in the non-rotating limit ($Ek^{-1} \to 0$) (see the discussion in Ünlüata & Mei (1970) and Xu & Bowen (1994)). In this unphysical limit, the predicted trajectory is at a 45° angle from the wave direction, as opposed to the 0° angle predicted by Stokes drift (figure 2*a*).

### 3.2. *Forced–steady model*

Still neglecting all time dependence (steady), Weber (1983) considers an oscillating normal wind stress to compensate for the viscous attenuation, resulting in

$$\overline{\overline{U}}_L(z) = \frac{u_S|_{z=0}}{\sqrt{2\mathrm{i}\, Ek^{-1}}}\left(1 - \frac{1}{1 - 2\mathrm{i}\, Ek^{-1}}\right)\mathrm{e}^{(1+\mathrm{i})z/\delta_E} + \frac{u_S(z)}{1 - 2\mathrm{i}\, Ek^{-1}}. \tag{3.3}$$

The difference between the unforced (3.2) and forced (3.3) models for the angle of the trajectories is small (figure 2*b–d*) except in the non-rotating limit (figure 2*a*). The Lagrangian-mean velocity corresponding to (3.3) reduces to the Stokes drift in the non-rotating limit (i.e. $\overline{\overline{\boldsymbol{u}}}_E \to 0$ as $Ek^{-1} \to 0$) instead of tending to infinity as in the unforced–steady model (3.2) and predicts smaller drift magnitudes (figure 3). The forced–steady model (3.3) also predicts complete compensation of the Stokes drift by the 'anti-Stokes drift' in the rapid-rotation limit (i.e. $|\overline{\overline{\boldsymbol{u}}}_L| \to 0$ as $Ek^{-1} \to \infty$).

### 3.3. *Unforced–unsteady model*

Under the same assumptions as Madsen (1978) but allowing variations on inertial time scales, Higgins *et al.* (2020) obtained an unsteady solution for the wave-induced Lagrangian-mean velocity:

$$\begin{aligned}\overline{U}_L(z,t) &= u_S|_{z=0} * K(z,t) + u_S(z,t=0),\\ &= \int_0^t u_S|_{z=0}(\tau)K(z,t-\tau)\mathrm{d}\tau + u_S(z,t=0),\end{aligned} \tag{3.4}$$

where $*$ denotes a convolution operation in time and the kernel is given by

$$K(z,t) = 2k\sqrt{\nu}\mathrm{e}^{-\mathrm{i}ft}\frac{\mathrm{e}^{-z^2/(4\nu t)}}{\sqrt{\pi t}} - \mathrm{i}f\mathrm{e}^{-\mathrm{i}ft}\frac{\mathrm{e}^{-z^2/(4\nu t)}}{2}\sum_{\pm}\mathrm{erfcx}\left(\sqrt{4k^2\nu t} \pm \frac{z}{\sqrt{4\nu t}}\right). \tag{3.5}$$

Equations (3.4)–(3.5) require an initial condition. Higgins *et al.* (2020) assume $\overline{U}_L(z, t = 0) = u_S(z, t = 0)$. Hence, the unsteady solution consists of an initial transient and a steady state.

The unforced–unsteady model (3.4)–(3.5) predicts that particles describe loops at the inertial period (so-called inertial circles) as they undergo an average (inertial-period-averaged) drift equal to that of the unforced–steady model (3.2) (figure 2*b–d*).

## 4. Results

Due to the slow rotation rate ($2\Omega/\omega \ll 1$), the waves produced by the wavemaker are quite similar to the waves in the case without background rotation. The observed effect of rotation is a modulation of the wave amplitude that increases with $\Omega$. This modulation is reported as a standard deviation in the average amplitude of between 3 % and 17 %

in table 1; more details are given in Appendix B. Hence, due to the small difference, we consider the waves as if they were not affected by rotation, and we treat, in our analysis, the effects of rotation on the wave field as a measurement error in the amplitude, which in turn determines the error in the estimated Stokes drift.

### 4.1. *Particle trajectories*

To compare theory and experiments, figure 2 shows examples of measured particle trajectories for waves with $f_w = 2.6$ Hz and four different (inverse) wave Ekman numbers $Ek^{-1}$. Without rotation, the measured trajectories are in the direction of the waves, as expected from the Stokes drift (figure 2*e*). Under counterclockwise rotation ($\Omega > 0$), the trajectories show an angle to the right of the wave direction for both theory and experiment. Additionally, for higher rotation rates (figure 2*g*,*h*), the measured trajectories show loops corresponding to inertial circles (the very small-scale oscillatory motion corresponds to the surface waves). With increasing rotation rate, the size of the inertial circles decreases, while their number increases. Rotating clockwise instead of counterclockwise leads to a drift to the left of the wave direction, as expected.

Some differences between experiments and theory are evident. Inertial circles are not observed at the lower rotation rates (figure 2*f*). The finite domain of the tank clearly restricts the validity of the theory for lower rotation rates: the trajectory predicted by the unforced–unsteady model in figure 2(*b*) shows an inertial circle that is wider than the width of the tank. To estimate this finite-domain effect, we calculate the finite-domain ratio $R = W/d_{circle}$, where $W$ is the width of the tank and $d_{circle} = |\boldsymbol{u}_S|/\Omega$ is the diameter of an inertial circle. For experiments in which inertial circles are not observed (lower rotation rates), $R < 2$. For experiments with clearly observable inertial circles (higher rotation rates), $R > 3$.

### 4.2. *Average drift speed*

For individual trajectories, it is difficult to quantitatively compare theory and experiments for several reasons. One of these is the spatial and temporal variation of the wave field (see Appendix B). To make a quantitative comparison with theory, we calculate the average drift speed by averaging over the full trajectory for each particle and over all the particles for each experiment (see Appendix A.3). Combining the drift velocities gives an average drift speed and a standard deviation. Each data point in figure 3 thus obtained is based on between 101 and 485 particles, with a median of 125 particles. The measured drift is repeatable, and there is no trend in the average drift speed over time (see figure 6 in Appendix C).

Figure 3(*a*) shows the normalised average drift speed $|\overline{\overline{\boldsymbol{u}}}_L|$ as a function of the (inverse) wave Ekman number. Measurements clearly show a non-zero drift speed, which decreases with increasing rotation rate in accordance with both the unforced–steady and the forced–steady theories. Rotation thus chokes Lagrangian-mean drift (i.e. anti-Stokes drift). At high (inverse) wave Ekman numbers ($Ek^{-1} \gtrsim 65$), the value of the average measured drift speed in figure 3(*a*) is in closer agreement with the unforced–steady compared to the forced–steady model. For low (inverse) wave Ekman numbers ($Ek^{-1} \lesssim 35$), the deviation between experiments and both steady models is most obvious, as can be explained by the unsteadiness of the drift on inertial time scales.

#### 4.2.1. *Unsteadiness and finite-domain effects*

For low (inverse) wave Ekman numbers ($Ek^{-1} \lesssim 35$), the typical time a particle stays within the region of interest (where drift is measured) $\Delta t_{trajectory}$ is relatively short

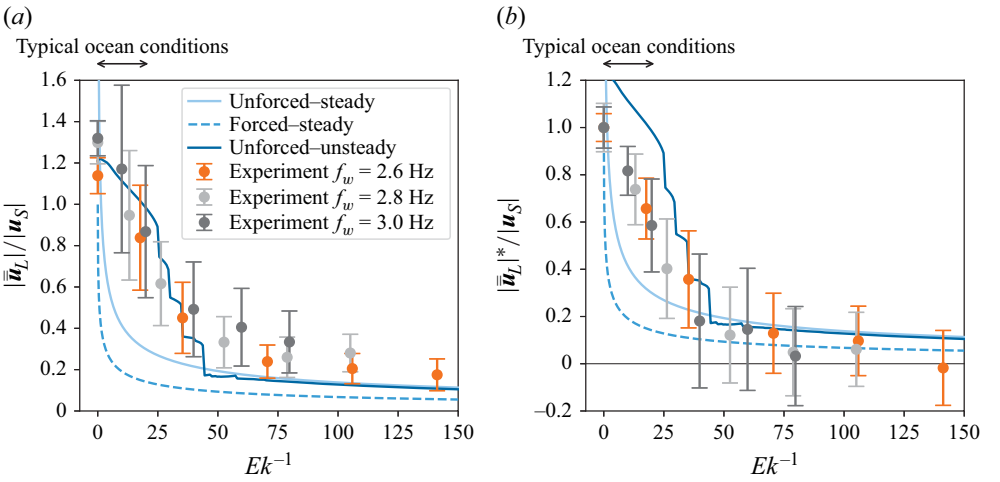


Figure 3. Comparison between experiments and theory for the average drift speed at the surface $|\overline{\overline{u}}_L|$ ($a$) and the modified average drift speed $|\overline{\overline{u}}_L|^* = |\overline{\overline{u}}_L| - |\overline{\overline{u}}_L|_{Ek^{-1}=0} + |u_S|$ ($b$) normalised by the predicted Stokes drift $|u_S|$ and shown as a function of the (inverse) wave Ekman number $Ek^{-1} = \Omega/(4\nu k^2)$. The error bar, which corresponds to ± one standard deviation, is defined in Appendix B.

compared with the rotation period $2\pi/\Omega$ (i.e. $\Delta t_{trajectory} \leqslant 2\pi/\Omega$). The average drift for these experiments is, therefore, not averaged over the inertial time scale, leading to an underestimation of the measured drift by both steady models. To account for this, we use the unforced–unsteady model (§ 3.3) to calculate theoretical trajectories for particles at each of the four dropping locations and estimate the average drift within the region of interest in the same way as for the experiments. The theoretical prediction thus obtained significantly improves agreement with experiments in figure 3($a$) for low (inverse) wave Ekman numbers. The irregularity in the resulting curve is an artefact of averaging over trajectories starting at only four particle-dropping locations, resulting in inertial circles that lie just inside or just outside the region of interest, over which the average is calculated.

#### 4.2.2. *Eulerian-mean 'return flow': modified average drift*

The theories described in § 3 were developed for the open ocean and therefore assume an infinite spatial domain. However, a laboratory wave flume has both finite-length and lateral boundaries. Without rotation, there is transport in the direction of the beach, i.e. towards the end of the flume, and due to mass conservation, a Eulerian-mean 'return flow' must somehow arise. Under rotation, transport occurs at an angle with respect to along-flume direction, and hence the Eulerian-mean return flow should also occur at an angle, implying that a three-dimensional Eulerian-mean circulation is set up inside the tank in the presence of rotation.

When comparing experiments with theory, it is clear from figure 3($a$) that the measured drift without rotation ($Ek^{-1} = 0$) is larger than the theoretical estimate of the Stokes drift (i.e. $|\overline{\overline{u}}_L|/|u_S| > 1$). This suggests a positive wave-induced Eulerian-mean flow in the $x$ direction at the surface, contrary to the negative 'return' flow that might be expected. Wave-induced Eulerian-mean flows have resulted in considerable difficulty in reconciling laboratory experiments with theory without rotation (van den Bremer *et al.* 2019; Monismith 2020). Although not the focus of this paper, different phenomena could explain what we observe, such as the effect of high wave steepness on the wave-driven surface

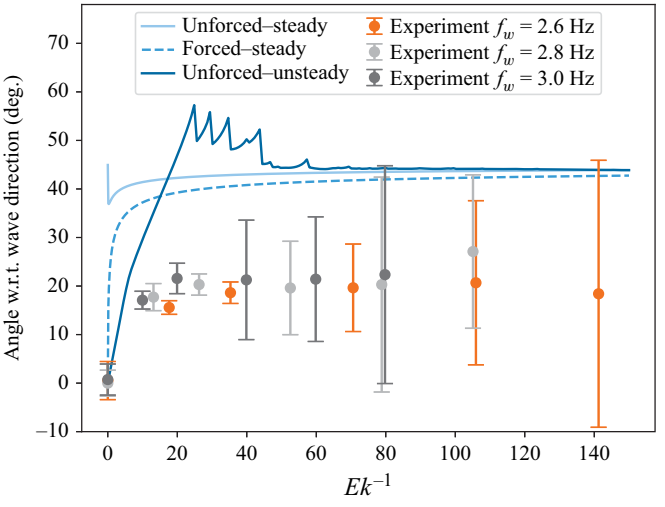


Figure 4. The magnitude of the angle of the drift with respect to the wave direction (directed to the right for counterclockwise rotation and to the left for clockwise rotation). The unforced–unsteady prediction shows the average angle based on theoretical drift within the interest region of particles dropped at the four dropping locations.

boundary layer (Grue & Kolaas 2017) or the vertical structure of the return flow, which are not included in the theoretical models considered here.

To obtain an estimate of this effect on our results, we adjust the measured drift speed, so that the modified drift for the non-rotating experiment is equal to the Stokes drift by definition (as done in Calvert *et al.* (2024)): $|\overline{\overline{\boldsymbol{u}}}_L|^* = |\overline{\overline{\boldsymbol{u}}}_L| - |\overline{\overline{\boldsymbol{u}}}_L|_{Ek^{-1}=0} + |\boldsymbol{u}_S|$. We note that there is no *a priori* reason why this modification is valid for the rotating experiments, although it should give an indication of the potential magnitude of the effect of the return flow. Figure 3(*b*) shows that the agreement between the two steady models and the experiments is generally improved by the modification, which also increases the error bars (see Appendix B). The agreement with the unforced–unsteady model is worsened somewhat, leading to an overestimation for low (inverse) wave Ekman numbers ($Ek^{-1} \lesssim 35$).

### 4.2.3. *Average drift angle*

The measured trajectories can also be used to estimate the average drift angle with respect to the wave direction. For each particle a linear fit through the $x$ position over time leads to the average drift velocity in the $x$ direction. Similarly, a linear fit through the $y$ position over time leads to the average drift velocity in the $y$ direction. Combining the angle between the velocity components of particles subject to the same wave condition and rotation rate gives the average angle with standard deviation as a function of the (inverse) wave Ekman number $Ek^{-1}$ (see figure 4). The irregularity in the unforced–unsteady curve in figure 4 is an artefact of averaging over trajectories starting at only four particle-dropping locations (the same as for the unforced–unsteady curve in figure 3*a*).

The angle obtained for experiments with rotation is $20° \pm 4°$ ($18° \pm 1°$ for $Ek^{-1} =$ 10–35 and $21° \pm 6°$ for $Ek^{-1} = 40$–141), which is approximately half of the 37°–44° angle predicted by the steady theories for $10 \lesssim Ek^{-1} \lesssim 141$. This discrepancy cannot be explained by the unsteady model and could be an effect of the finite width of the experimental set-up. For context, we note that the standard deviation of the angle measurements from a single experiment is very large for high (inverse) wave Ekman numbers ($\pm 9°$ to $\pm 28°$ for $Ek^{-1} \gtrsim 40$).

## 5. Discussion and conclusions

This paper has examined the effect of rotation on surface wave-induced drift in laboratory experiments. All the effects of rotation predicted by theory are observed. First, the Lagrangian-mean (wave-averaged) particle trajectories describe inertial circles, which become evident at larger (inverse) wave Ekman numbers ($Ek^{-1} = \Omega/(4\nu k^2) \gtrsim 65$). Second, when averaged over the inertial period, the Lagrangian-mean drift is to the right of the wave direction for counterclockwise rotation and reduces in magnitude with increasing (inverse) wave Ekman number. Our laboratory experiments thus provide the first experimental observation of reduced wave-induced drift in a rotating reference frame in line with the classical anti-Stokes drift phenomenon, whereby the Coriolis–Stokes force leads to an Eulerian-mean flow that is equal and opposite to the Stokes drift (Ursell 1950; Hasselmann 1970).

The magnitude of the average drift observed is generally larger than predicted by the 'unforced' (Madsen 1978) and the 'forced' (Weber 1983) steady-state models for the wave-induced Eulerian-mean flow. Of these two models, the 'unforced' model agrees somewhat better with measurements, but this model is singular in the non-rotating limit. The 'forced' model does not have this problem, but it does assume a pressure normal to the surface to sustain the wave field, which is not present in experiments. For low (inverse) wave Ekman numbers ($Ek^{-1} \lesssim 35$), the disagreement between the experiment and the steady-state models is greatest. This is the result of the finite domain of the experiment and the unsteadiness of the drift on inertial time scales. The unsteady model of Higgins *et al.* (2020) leads to much better agreement with measurements in this regime. While the unsteady model improves agreement with experiments for low (inverse) wave Ekman number, it does not account for the effect of the tank boundaries on the flow itself. We note that at these lower (inverse) wave Ekman numbers, no inertial circles are visible in the trajectories in contrast to theory (figure 2). While we find reasonable agreement for the drift speed, the angle between the average drift and the direction of the waves in our measurements is only half of that predicted by theory, which could also be a result of the finite tank width.

Without rotation ($Ek^{-1} = 0$), the measured drift is larger than the theoretical estimate of the Stokes drift (i.e. $|\overline{\overline{\boldsymbol{u}}}_L|/|\boldsymbol{u}_S| > 1$), suggesting a positive instead of a negative wave-induced Eulerian-mean flow (cf. 'return flow'). We note that wave-induced Eulerian-mean flows have led to considerable difficulty in previous experiments (Monismith *et al.* 2007; van den Bremer & Breivik 2017; Monismith 2020). Correcting for this flow is, therefore, often necessary (Calvert *et al.* 2024). Using the additional drift observed at zero rotation to adjust the measured drift in experiments with rotation results in better agreement, except for small (inverse) wave Ekman numbers, where the effects of unsteadiness are important. Whether this additional drift arises because of the effects of high wave nonlinearity on the wave-induced surface boundary layer (Grue & Kolaas 2017) or non-uniformity of the return flow and the effect of the beach on this (Li & Dalrymple 1998) should be studied in future experiments measuring the vertical (and horizontal) structure of the Eulerian-mean and Lagrangian-mean velocities. Extending current theories to include the finite length and lateral boundaries of a wave flume would also further improve our understanding of the potentially complex three-dimensional Eulerian-mean flow under rotation.

There are several relevant time scales in the experiment, besides the time scale of rotation. Longuet-Higgins (1953) describes two possibilities for the transport of vorticity to the interior of the fluid. In the convective solution the vorticity is transported from the beach and/or wavemaker with the mass transport velocity. The associated advection time scale $L/U$ is of the order of minutes for our experiment (using the length of the flume and

the measured drift velocity). In the conduction solution, vorticity is transported from the (viscous) boundary layers at the bottom and top of the fluid. The corresponding viscous time scale is given by $L^2/\nu$. Choosing the Stokes depth as the length scale gives $1/(4k^2\nu)$, which is of the order of minutes in our experiments. Using the water depth instead provides a much longer time scale of $h^2/\nu = 375$ min. The drift measurements took place after the advection time scale and the shortest viscous time scale, but before the longest viscous time scale. We note, however, that in a rotating system the relevant time scale might be the Ekman time scale, which is of the order of 4–11 min, rather than the viscous time scales discussed above. No significant differences in the average drift can be observed between the videos taken at different moments over the first hour (see figure 6 in Appendix C). The potential time evolution of the drift on longer time scales can be a topic of investigation in future experiments.

A crucial element in finding agreement between theory and experiments is found to be the unsteadiness of drift on rotational time scales. However, the unforced–unsteady model by Higgins *et al.* (2020) remains singular in the non-rotating steady limit. Future work should remedy this by using a more representative surface boundary condition of the laboratory or the field (Weber 2019). Although assuming a constant viscosity equal to the molecular viscosity may be reasonable for our laboratory experiment, a (depth-dependent) eddy viscosity would more accurately represent the turbulence in the upper-ocean boundary layer (Mellor & Yamada 1982). Extending the unsteady theory of Higgins *et al.* (2020) to allow a depth-dependent eddy viscosity would enable improved prediction of wave-induced transport, also noting the importance for drift of the near-surface vertical structure of the velocity as observed in the field (Laxague *et al.* 2018). A numerical simulation of the wave flume experiment with a method similar to that of Xuan, Deng & Shen (2024) would provide further insight into the effect of turbulence and depth-dependent turbulent viscosity on the wave-induced drift.

To assess the implications of our findings for the ocean, the range of (inverse) wave Ekman numbers for typical ocean conditions is indicated by the horizontal black arrows in figure 3 (the largest value of $Ek^{-1} = 20$ corresponds to a 12 s wave, $f = 1.4 \times 10^{-4}$ rad $\mathrm{s}^{-1}$ and an eddy viscosity of $10^{-3}$ $\mathrm{m}^2\,\mathrm{s}^{-1}$; using a smaller viscosity would yield much larger values). At these (inverse) wave Ekman numbers, a significant reduction of the wave-induced drift due to the Earth's rotation is expected. This effect is often not taken into account in particle tracking simulations, unless Eulerian-mean flows are obtained from a coupled wave–ocean model (Drivdal *et al.* 2014; Rühs *et al.* 2024), leading to a drift prediction that is too large and in the wrong direction. As realistic wave fields vary temporally on time scales similar to the inertial period (e.g. due to storms), including the effects of unsteadiness of the wave-induced Eulerian-mean flow will be as important in the field as in our experiments. To be applicable to the ocean, the turbulent eddy viscosity and additional drift due to wave breaking (Pizzo, Melville & Deike 2019) should also be taken into account.

**Supplementary movie.** Supplementary movie is available at https://doi.org/10.1017/jfm.2025.10476

**Acknowledgements.** The authors would like to thank D. de Gans and L. Middelplaats from Dienst Elektronische en Mechanische Ontwikkeling (DEMO) at Delft University of Technology as well as P. van der Gaag, C. Willems, A. van der Vlies and A. Doorn from Delft University of Technology for designing and building the wave flume set-up. We would also like to thank F. van Uittert and G. Oerlemans from Eindhoven University of Technology for their support in conducting the experiment.

**Funding.** This research received no specific grant from any funding agency, commercial or not-for-profit sectors.

| Rotation rate $\Omega$ (rad s$^{-1}$) | Rotation period $T$ (s) | Spin-up time $5t_E$ (min) | Rossby radius $\mathcal{R}$ (m) |
|---|---|---|---|
| 0.4189 | 15 | 19 | 1.44 |
| 0.3142 | 20 | 22 | 1.92 |
| 0.2094 | 30 | 27 | 2.89 |
| 0.1047 | 60 | 39 | 5.79 |
| 0.0524 | 120 | 55 | 11.57 |

Table 2. The spin-up time and the Rossby radius of deformation $\mathcal{R} = \sqrt{gh}/2\Omega$ for each (non-zero) rotation rate used in the experiment.

**Declaration of interests.** The authors report no conflict of interest.

**Data availability statement.** The dataset containing all software and processed data underlying this publication is available at the 4TU.ResearchData repository: https://doi.org/10.4121/00e933f9-1e70-4c39-8516-52f295cfe166. This dataset also contains all the raw data required to reproduce figure 2.

## Appendix A. Experimental methodology

### A.1. *Spin-up time*

The values for the spin-up times used in the experiment are given in table 2.

### A.2. *Timeline of measurement procedure*

The timeline of the measurement procedure for each experiment is shown in figure 5.

### A.3. *Data processing*

A particle is first recognised in a video when a detected yellow area is larger than 11.8 px$^2$ and it is located within a region of 565 $\times$ 1840 pixels around the dropping system. A new particle search is started every 2, 1.5 and 1 s for experiments with wave frequencies of 2.6, 2.8 and 3 Hz, respectively. A rectangular box of 44 $\times$ 25 pixels is drawn around each particle. Duplicates are removed when the centres of two boxes are closer than two times the diameter of the particles. The boxes are then tracked with the CSRT algorithm using the OpenCV Python library (version 4.9.0.80) throughout the remainder of the video.

To correct for camera distortion, we use images of a calibration chequerboard with 15 mm squares floating on the water surface at positions covering the entire measurement area. The pinhole camera model with an image of the calibration board at a known location in the flume is then used to transform the undistorted pixel positions of the particles to real-world positions (in mm).

We remove the beginning and end of a track when outside the region of interest (5 cm away from each of the sidewalls). When two particles get too close together the tracking box can jump to the other particle. These erroneous tracks are excluded by removing the rest of the track for both particles from the moment the distance between the tracking boxes is within half the width and height of the box. Additionally, tracks that are too short are discarded to be able to calculate a meaningful average drift velocity. The minimal track length is 20, 15 and 12 s for experiments with wave frequencies of 2.6, 2.8 and 3 Hz, respectively.

The average drift speed per particle is computed from its trajectory by performing a linear fit through the distance travelled as a function of time. Combining the drift velocities of individual particles from experiments with the same rotation rate and wave conditions

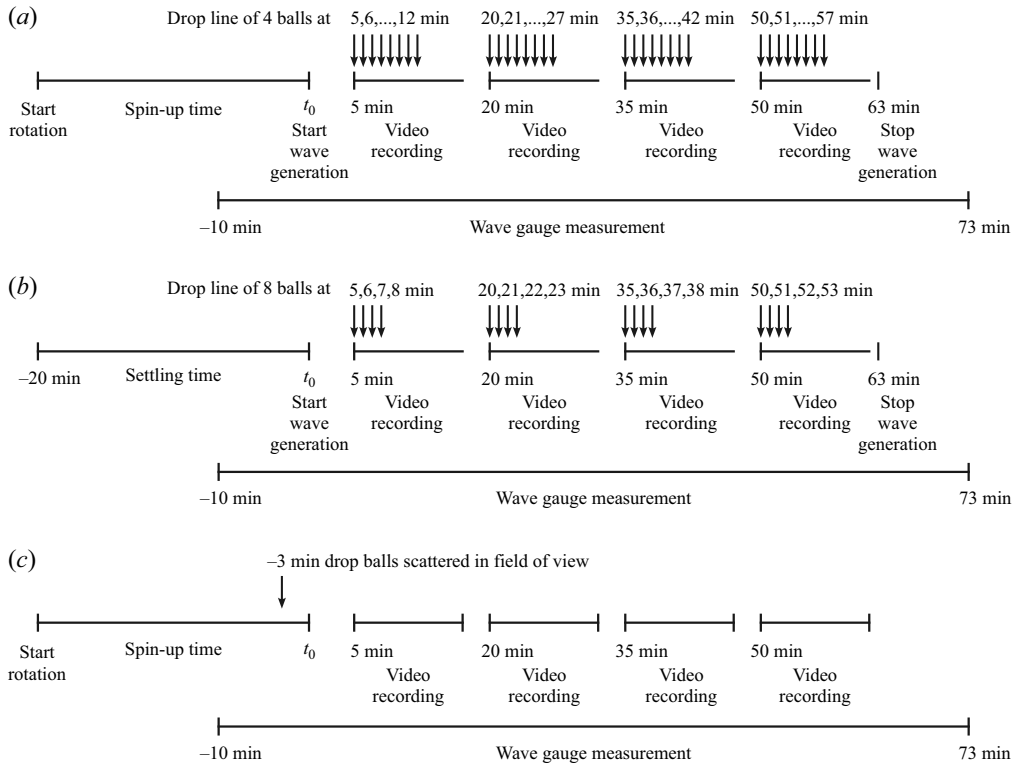


Figure 5. Timeline for (*a*) experiments with both rotation and wave generation, (*b*) experiments without rotation, but with wave generation and (*c*) experiments with rotation, but without wave generation.

gives an average drift speed and a standard deviation as a function of (inverse) wave Ekman number.

## Appendix B. Measurement error

There are several sources of error for the measured average drift. First, the (time-averaged) wave amplitude measured at each of the seven wave gauges is slightly different. This causes a standard deviation in the average amplitude between 3 % and 17 % (see table 1). At higher rotation rates there is also a time variation in the amplitude. The surface elevation shows groups, causing the wave amplitude to be modulated. The standard deviation of the amplitudes measured at the different wave gauges $\sigma_a$ (given in table 1) can be used to estimate the error in the average measured amplitude $a$, used to calculate the Stokes drift $|\boldsymbol{u}_S|$. Similarly, the error in the average drift velocity $|\overline{\boldsymbol{u}}_L|$ can be estimated by the standard deviation of the measured drift velocity of individual particles subject to the same wave condition and rotation rate $\sigma_{|\overline{\boldsymbol{u}}_L|}$. The error in the normalised average drift $|\overline{\boldsymbol{u}}_L|/|\boldsymbol{u}_S|$ is then given by

$$\sigma_{|\overline{\boldsymbol{u}}_L|/|\boldsymbol{u}_S|} = \frac{1}{|\boldsymbol{u}_S|}\sqrt{\sigma^2_{|\overline{\boldsymbol{u}}_L|} + 4|\overline{\boldsymbol{u}}_L|^2\,\frac{\sigma_a^2}{a^2}}, \tag{B1}$$

where we assume independent variables. This error is shown as the error bars on the data points in figure 3(*a*). The error in the modified normalised average drift $|\overline{\boldsymbol{u}}_L|^*/|\boldsymbol{u}_S| =$

$(|\overline{\boldsymbol{u}}_L| - |\overline{\overline{\boldsymbol{u}}}_L|_{Ek^{-1}=0} + |\boldsymbol{u}_S|)/|\boldsymbol{u}_S|$, shown as the error bars on the data points in figure 3(*b*), is similarly given by

$$\sigma_{|\overline{\boldsymbol{u}}_L|^*/|\boldsymbol{u}_S|} = \frac{1}{|\boldsymbol{u}_S|}\sqrt{\sigma^2_{|\overline{\boldsymbol{u}}_L|} + \sigma^2_{|\overline{\boldsymbol{u}}_L|_{Ek^{-1}=0}} + 4\left(|\overline{\boldsymbol{u}}_L| - |\overline{\boldsymbol{u}}_L|_{Ek^{-1}=0}\right)^2 \frac{\sigma_a^2}{a^2}}, \tag{B2}$$

where $\sigma_{|\overline{\boldsymbol{u}}_L|_{Ek^{-1}=0}}$ is the error in the average drift velocity measured at zero rotation.

The observed particle drift is influenced by any background motion. When spinning up the set-up from zero rotation to the desired rotation rate, a series of recirculation cells forms (van Heijst, Davies & Davis 1990). A spin-up time of $5t_E$ was used to allow this flow to dissipate and minimise the residual motion during the experiment. Experiments without wave generation are conducted to assess the remaining background motion at the time of the wave-induced drift measurements. The experimental procedure and data processing for these experiments are the same as those for the experiments with wave generation. The only difference is that particles are dropped throughout the full field of view of the camera 8 min before the start of the first measurement. As a consequence, the experiment is conducted without a lid above the measurement zone. The average drift caused by the background motion is found to be 0.2–0.8 mm $\mathrm{s}^{-1}$. This is 1.0 %–5.5 % of the drift velocity with wave generation at the same rotation rate.

Additionally, the surface elevation without wave generation shows an oscillation with the rotation period which does not decay over time. This oscillation has an amplitude of approximately $0.2 \pm 0.05$ mm (less than 3 % of the wave amplitude). Similar oscillations have been observed in other rotating experiments (e.g. Boisson *et al.* 2012; Rajaei *et al.* 2018). In our experiment, this oscillation is most likely caused by a slight precession of the table. However, the background rotation of the Earth also causes a precession, which means that these oscillations are unavoidable and a perfect solid-body rotation can never be reached (Boisson *et al.* 2012; Rajaei *et al.* 2018).

It should be noted that, in one experiment without rotation and with $f_w = 2.6$ Hz, the measured drift velocity decreased at approximately 15 cm before the beach. This experiment was reprocessed such that only the tracks before this point where used (up to 0.87 m from the wavemaker), effectively making the region of interest for this measurement smaller in the $x$ direction. The value of the drift within this modified region is consistent with the drift value in the full region of interest for other experiments.

## Appendix C. Repeatability

The difference between the average drift velocity of each video and the average drift velocity of all particles subject to the same wave condition and rotation rate is less than 88 % of the standard deviation of the individual drift velocities in the video, with an average of 20 % (see figure 6). This means that the experiment is repeatable and each video with the same rotation rate and wave condition can be considered a repeat. Some of these experiments were conducted without wave gauges. The presence of the wave gauges, therefore, does not noticeably change the observed average drift velocity. Clockwise rotation changes the direction of the drift, but the value of the average drift velocity is equivalent to the drift velocity for counterclockwise rotation. It can, therefore, be taken into account when calculating the average drift velocity for $\Omega = 0.4189$ rad $\mathrm{s}^{-1}$ and $f_w = 2.6$ Hz. No trend over time can be observed in the drift velocity for videos taken at different times since the start of the wavemaker (see figure 6).

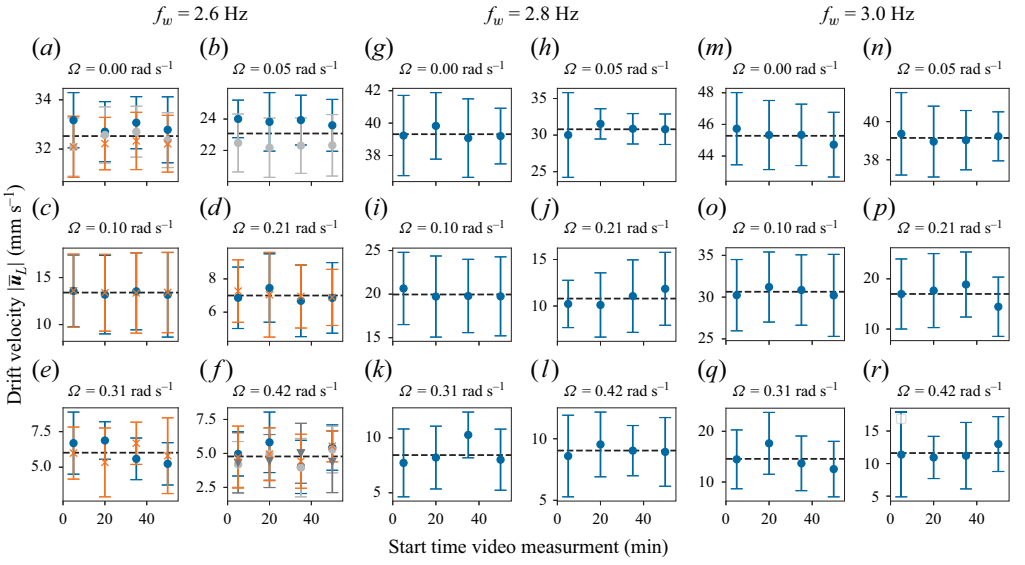


Figure 6. Average drift velocity with standard deviation for each video. An (orange) cross indicates a measurement without wave gauges in the set-up. A (dark grey) triangle indicates a measurement with the same absolute value of the rotation rate, but rotating in the opposite direction (clockwise). The dashed line shows the drift velocity averaged over all measurements with the same rotation rate and wave condition.

## References


Ardhuin, F., Marié, L., Rascle, N., Forget, P. & Roland, A. 2009 Observation and estimation of Lagrangian, Stokes, and Eulerian currents induced by wind and waves at the sea surface. *J. Phys. Oceanogr.* **39** (11), 2820–2838.

Boisson, J., Cébron, D., Moisy, F. & Cortet, P.-P. 2012 Earth rotation prevents exact solid-body rotation of fluids in the laboratory. *Europhys. Lett.* **98** (5), 59002.

Breivik, Ø., Allen, A.A., Maisondieu, C. & Olagnon, M. 2013 Advances in search and rescue at sea. *Ocean Dyn.* **63** (1), 83–88.

van den Bremer, T.S. & Breivik, Ø. 2017 Stokes drift. *Phil. Trans. R. Soc. A Math. Phys. Engng Sci.* **376**, 20170104.

van den Bremer, T.S., Whittaker, C., Calvert, R., Raby, A. & Taylor, P.H. 2019 Experimental study of particle trajectories below deep-water surface gravity wave groups. *J. Fluid Mech.* **879**, 168–186.

Calvert, R., Peytavin, A., Pham, Y., Duhamel, A., van der Zanden, J., van Essen, S.M., Sainte-Rose, B. & van den Bremer, T.S. 2024 A laboratory study of the effects of size, density, and shape on the wave-induced transport of floating marine litter. *J. Geophys. Res. Oceans* **129** (7), e2023JC020661.

Craik, A.D.D. & Leibovich, S. 1976 A rational model for Langmuir circulations. *J. Fluid Mech.* **73** (3), 401–426.

Cunningham, H.J., Higgins, C. & van den Bremer, T.S. 2022 The role of the unsteady surface wave-driven Ekman–Stokes flow in the accumulation of floating marine litter. *J. Geophys. Res. Oceans* **127** (6), e2021JC018106.

Dobler, D., Huck, T., Maes, C., Grima, N., Blanke, B., Martinez, E. & Ardhuin, F. 2019 Large impact of Stokes drift on the fate of surface floating debris in the South Indian Basin. *Mar. Pollut. Bull.* **148**, 202–209.

Drivdal, M., Broström, G. & Christensen, K.H. 2014 Wave-induced mixing and transport of buoyant particles: application to the Statfjord A oil spill. *Ocean Sci.* **10**, 977–991.

Fraser, C.I., Morrison, A.K., Hogg, A.McC., Macaya, E.C., van Sebille, E., Ryan, P.G., Padovan, A., Jack, C., Valdivia, N. & Waters, J.M. 2018 Antarctica's ecological isolation will be broken by storm-driven dispersal and warming. *Nat. Clim. Change* **8**, 704–708.

Greenspan, H.P. & Howard, L.N. 1963 On a time-dependent motion of a rotating fluid. *J. Fluid Mech.* **17** (3), 385.

Gruber, N., Lachkar, Z., Frenzel, H., Marchesiello, P., Münnich, M., McWilliams, J.C., Nagai, T. & Plattner, G.-K. 2011 Eddy-induced reduction of biological production in eastern boundary upwelling systems. *Nat. Geosci.* **4** (11), 787–792.

GRUE, J. & KOLAAS, J. 2017 Experimental particle paths and drift velocity in steep waves at finite water depth. *J. Fluid Mech.* **810**, R1.
HASSELMANN, K. 1970 Wave-driven inertial oscillations. *Geophys. Fluid Dyn.* **1** (3-4), 463–502.
VAN HEIJST, G.J.F., DAVIES, P.A. & DAVIS, R.G. 1990 Spin-up in a rectangular container. *Phys. Fluids A Fluid Dyn.* **2** (2), 150–159.
HIGGINS, C., VANNESTE, J. & VAN DEN BREMER, T.S. 2020 Unsteady Ekman–Stokes dynamics: implications for surface wave-induced drift of floating marine litter. *Geophys. Res. Lett.* **47** (18), e2020GL089189.
HUANG, N.E. 1979 On surface drift currents in the ocean. *J. Fluid Mech.* **91** (1), 191–208.
LAXAGUE, N.J.M., Ö-ZGÖKMEN, T.M., HAUS, B.K., NOVELLI, G., SHCHERBINA, A., *et al.* 2018 Observations of near-surface current shear help describe oceanic oil and plastic transport. *Geophys. Res. Lett.* **45**, 245–249.
LENAIN, L., PIZZO, N. & MELVILLE, W.K. 2019 Laboratory studies of Lagrangian transport by breaking surface waves. *J. Fluid Mech.* **876**, R1.
LENTZ, S.J., FEWINGS, M., HOWD, P., FREDERICKS, J. & HATHAWAY, K. 2008 Observations and a model of undertow over the inner continental shelf. *J. Phys. Oceanogr.* **38** (11), 2341–2357.
LENTZ, S.J. & FEWINGS, M.R. 2012 The wind- and wave-driven inner-shelf circulation. *Annu. Rev. Mar. Sci.* **4**, 317–343.
LI, L. & DALRYMPLE, R.A. 1998 Instabilities of the undertow. *J. Fluid Mech.* **369**, 175–190.
LONGUET-HIGGINS, M.S. 1953 Mass transport in water waves. *Phil. Trans. R. Soc. Lond. A Math. Phys. Sci.* **245** (903), 535–581.
LONGUET-HIGGINS, M.S. & STEWART, R.W. 1962 Radiation stress and mass transport in gravity waves, with application to surf beats. *J. Fluid Mech.* **13** (4), 481–504.
MADSEN, O.S. 1978 Mass transport in deep-water waves. *J. Phys. Oceanogr.* **8** (6), 1009–1015.
MCINTYRE, M.E. 1981 On the wave momentum myth. *J. Fluid Mech.* **106**, 331–347.
MELLOR, G.L. & YAMADA, T. 1982 Development of a turbulence closure model for geophysical fluid problems. *Rev. Geophys.* **20** (4), 851–875.
MONISMITH, S.G. 2020 Stokes drift: theory and experiments. *J. Fluid Mech.* **884**, F1.
MONISMITH, S.G., COWEN, E.A., NEPF, H.M., MAGNAUDET, J. & THAIS, L. 2007 Laboratory observations of mean flows under surface gravity waves. *J. Fluid Mech.* **573**, 131–147.
NIELSEN, P. 2006 Sheet flow sediment transport under waves with acceleration skewness and boundary layer streaming. *Coast. Eng.* **53** (9), 749–758.
NOOTEBOOM, P.D., BIJL, P.K., VAN SEBILLE, E., VON DER HEYDT, A.S. & DIJKSTRA, H.A. 2019 Transport bias by ocean currents in sedimentary microplankton assemblages: implications for paleoceanographic reconstructions. *Paleoceanogr. Paleoclimatol.* **34** (7), 1178–1194.
ONINK, V., WICHMANN, D., DELANDMETER, P. & VAN SEBILLE, E. 2019 The role of Ekman currents, geostrophy, and stokes drift in the accumulation of floating microplastic. *J. Geophys. Res. Oceans* **124** (3), 1474–1490.
PAPROTA, M., SULISZ, W. & REDA, A. 2016 Experimental study of wave-induced mass transport. *J. Hydraul. Res.* **54** (4), 423–434.
PEARSON, B. 2018 Turbulence-induced anti-Stokes flow and the resulting limitations of large-Eddy simulation. *J. Phys. Oceanogr.* **48** (1), 17–122.
PHILLIPS, O.M. 1977 *The Dynamics of the Upper Ocean*, 2nd edn. Cambridge University Press.
PIZZO, N., MELVILLE, W.K. & DEIKE, L. 2019 Lagrangian transport by nonbreaking and breaking deep-water waves at the ocean surface. *J. Phys. Oceanogr.* **49** (4), 983–992.
POLLARD, R.T. 1970 Surface waves with rotation: an exact solution. *J. Geophys. Res.* **75** (30), 5895–5898.
RAJAEI, H., ALARDS, K.M.J., KUNNEN, R.P.J. & CLERCX, H.J.H. 2018 Velocity and acceleration statistics in rapidly rotating Rayleigh–Bénard convection. *J. Fluid Mech.* **857**, 374–397.
RÜHS, S., VAN DEN BREMER, T.S., CLEMENTI, E., DENES, M.C., MOULIN, A. & VAN SEBILLE, E. 2024 Non-negligible impact of Stokes drift and wave-driven Eulerian currents on simulated surface particle dispersal in the Mediterranean Sea. *EGUsphere* **2024**, 1–37.
RÖHRS, J., CHRISTENSEN, K.H., HOLE, L.R., BROSTRÖM, G., DRIVDAL, M. & SUNDBY, S. 2012 Observation-based evaluation of surface wave effects on currents and trajectory forecasts. *Ocean Dyn.* **62**, 1519–1533.
VAN SEBILLE, E. *et al.* 2020 The physical oceanography of the transport of floating marine debris. *Environ. Res. Lett.* **15** (2), 023003.
SESHASAYANAN, K. & GALLET, B. 2019 Surface gravity waves propagating in a rotating frame: The Ekman–Stokes instability. *Phys. Rev. Fluids* **4**, 104802.

SMITH, J.A. 2006 Observed variability of ocean wave Stokes drift, and the Eulerian response to passing groups. *J. Phys. Oceanogr.* **36** (7), 1381–1402.

STOKES, G.G. 1847 On the theory of oscillatory waves. *Trans. Camb. Phil. Soc.* **8**, 441–445.

SUTHERLAND, B.R., DIBENEDETTO, M., KAMINSKI, A. & VAN DEN BREMER, T.S. 2023 Fluid dynamics challenges in predicting plastic pollution transport in the ocean: a perspective. *Phys. Rev. Fluids* **8**, 070701.

SUZUKI, N. & FOX-KEMPER, B. 2016 Understanding Stokes forces in the wave-averaged equations. *J. Geophys. Res. Oceans* **121** (5), 3579–3596.

SWAN, C. & SLEATH, J.F.A. 1990 A second approximation to the time-mean Lagrangian drift beneath a series of progressive gravity waves. *Ocean Eng.* **17** (1), 65–79.

ÜNLÜATA, Ü. & MEI, C.C. 1970 Mass transport in water waves. *J. Geophys. Res.* **75** (36), 7611–7618, 1896.

URSELL, F. 1950 On the theoretical form of ocean swell on a rotating earth. *Geophys. J. Intl* **6** (s1), 1–8.

VALLIS, G.K. 2017 *Atmospheric and Oceanic Fluid Dynamics: Fundamentals and Large-Scale Circulation*, 2nd edn. Cambridge University Press.

WEBER, J.E. 1983 Steady wind- and wave-induced currents in the open ocean. *J. Phys. Oceanogr.* **13** (3), 524–530.

WEBER, J.E. 2019 Lagrangian studies of wave-induced flows in a viscous ocean. *Deep Sea Res. II Topical Stud. Oceanogr.* **160**, 68–81.

WEBER, J.E.H. 2011 Do we observe Gerstner waves in wave tank experiments? *Wave Motion* **48** (4), 301–309.

XU, Z. & BOWEN, A.J. 1994 Wave- and wind-driven flow in water of finite depth. *J. Phys. Oceanogr.* **24** (9), 1850–1866.

XUAN, A., DENG, B.-Q. & SHEN, L. 2024 Effect of an incoming gaussian wave packet on underlying turbulence. *J. Fluid Mech.* **999**, A45.